Lawrence Berkeley National Laboratory
LBL Publications

Title
The Chemical and Electronic Properties of Stability-Enhanced, Mixed Ir-TiO x Oxygen Evolution Reaction Catalysts

Permalink
https://escholarship.org/uc/item/83s3211t

Journal
ACS Catalysis, 13(23)

ISSN
2155-5435

Authors
van der Merwe, Marianne
Garcia-Diez, Raul
Lahn, Leopold
et al.

Publication Date
2023-12-01

DOI
10.1021/acscatal.3c02948

Copyright Information
This work is made available under the terms of a Creative Commons Attribution License, available at https://creativecommons.org/licenses/by/4.0/

Peer reviewed

eScholarship.org Powered by the California Digital Library
University of California

ACS Catalysis

Open Access
This article is licensed under CC-BY 4.0

pubs.acs.org/acscatalysis
Research Article

The Chemical and Electronic Properties of Stability-Enhanced, Mixed Ir-TiO_x Oxygen Evolution Reaction Catalysts

Marianne van der Merwe,* Raul Garcia-Diez, Leopold Lahn, R. Enggar Wibowo, Johannes Frisch, Mihaela Gorgoi, Wanli Yang, Shigenori Ueda, Regan G. Wilks, Olga Kasian, and Marcus Bär*

Cite This: ACS Catal. 2023, 13, 15427−15438
Read Online

ACCESS | Metrics & More | Article Recommendations | Supporting Information

ABSTRACT: Iridium has emerged as the leading catalyst material for the anodic oxygen evolution reaction (OER) in acidic media. Often, iridium is mixed with more stable materials such as titanium. For these materials, the electronic structure of titanium plays a crucial role since with varying degrees of oxidation titanium transforms to semiconducting or even insulating phases. Yet, the electronic properties of mixed Ir-TiO_x catalysts have never been systematically studied. In this study, we correlate the catalytic performance of mixed Ir-TiO_x-based OER catalysts with the electronic structure of the surface layers. For this, a thin film material library with a 20−70 at. % Ir (Ir/[Ir + Ti]) compositional gradient was prepared. We used inductively coupled plasma mass spectrometry to test the OER activity and stability of the set of mixed Ir-TiO_x catalyst candidate materials. Complementary, Ti $L_{2,3}$- and O K-edge X-ray absorption spectroscopy and depth-dependent X-ray photoelectron spectroscopy measurements were performed to correlate the catalytic performance with the composition and electronic property profiles of these mixed Ir-TiO_x OER anode catalysts. The spectroscopic analysis reveals that titanium is present as an intermixed matrix of semiconductive but stable TiO_2, conductive but less stable titanium-suboxides (TiO_x), and highly conductive but highly unstable metallic Ti(0). The extent of the titanium oxidation strongly depends on the titanium content, with a lower degree of oxidation observed for lower titanium (and thus higher iridium) contents. For an iridium loading of 70 at. %, the respective mixed Ir-TiO_x catalyst showed a similar OER activity to that of the pure metallic iridium (1.74 vs 1.59 V_{RHE}, respectively) but with a 71% lower iridium dissolution rate relative to the pure metallic iridium. This demonstrates the stabilization effect of titanium addition while maintaining high OER activity.

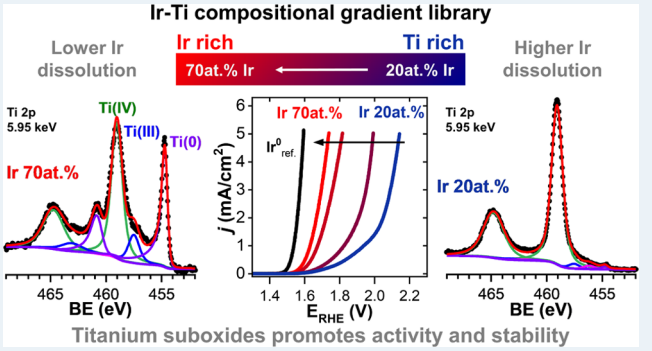

KEYWORDS: *oxygen evolution reaction, titanium suboxides, stability, mixed iridium−titanium catalysts, X-ray spectroscopy*

Downloaded via 108.75.79.166 on May 16, 2024 at 18:36:34 (UTC).
See https://pubs.acs.org/sharingguidelines for options on how to legitimately share published articles.

INTRODUCTION

The intermittent nature of renewable energy sources leaves the supply chain vulnerable to downtime periods (of no wind or sun), during which no electrical energy can be generated. Sustainable large-scale solutions for energy storage are therefore needed, and proton exchange membrane water electrolysis (PEM-WE) has gained attention as a promising technology for the on-site conversion of excess renewable electricity into oxygen and hydrogen.[1,−3] In PEM-WE, oxygen is generated under harsh acidic conditions through the oxygen evolution reaction (OER) occurring at the anode. Development of corrosion-resistant catalysts for the OER has proven particularly challenging, with few materials showing favorable activity and long-term stability against dissolution. Currently, only iridium oxide-based anode materials are used on a commercial basis.[4] However, both iridium and its oxides still undergo dissolution,[5,−10] challenging the resource management of this scarce noble metal to meet the ever increasing energy demands. Rutile iridium oxide (IrO_2), with metallic-type conductivity, displays lower activity but higher stability (2−3 orders of magnitude lower iridium dissolution) compared to its metallic form.[5] The significantly higher dissolution of metallic iridium is linked to the phase transition and formation of hydrous iridium oxide species on the surface. The amorphous iridium oxides (IrO_x) exhibit high catalytic activity while suffering from an increased dissolution rate. Most studies therefore focus on developing IrO_x/IrO_2 anode materials where activity and durability are balanced.

One well-demonstrated approach to increasing stability while simultaneously reducing iridium loading is mixing iridium oxide with other less active (but more stable)

Received: June 29, 2023
Revised: October 27, 2023
Accepted: October 27, 2023
Published: November 15, 2023

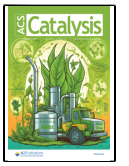

© 2023 The Authors. Published by American Chemical Society

materials, such as transition metal oxides, e.g., titanium or tin oxides.[11,12] However, in the design of such mixed catalyst materials, the charge transport pathways (that ensure sufficient electrical conductivity) become crucial parameters for the material's OER performance. Typically, due to the semi- or even nonconductive nature of stoichiometric titanium dioxide (TiO_2) and tin oxide (SnO_2), the electrical conductivity and OER performance of the material are determined solely by the nature of the interconnection between the conductive iridium oxide domains on the nonconductive support material. Without well-interconnected iridium dioxide domains in IrO_2/TiO_2 materials, high Ohmic losses occur resulting in poor OER performance.[13,14] Heat treatments also influence the electrical conductivity of the material by influencing the degree of crystallinity of the iridium and therefore its conductivity.[14] While studies investigated the effect of temperature treatments on the electrical properties of the iridium species, they do not address the nonconductive nature of the support material.

The electrical conductivity of the support material can be improved by doping the TiO_2 with materials such as niobium[15] or vanadium.[16] Another approach is the exploitation of conductive substoichiometric titanium oxide phases, such as Magnéli phases (Ti_nO_{2n-1} where $4 \leq n \leq 10$).[17,−23] The substoichiometric titania supports are more conductive[20,24] but less stable than TiO_2 during OER in acidic media given their thermodynamic instability under these conditions.[25] On a lab scale,[21] their lower stability is outweighed by the significantly improved electrical transport pathways between the supported iridium oxide and current collectors, thereby minimizing Ohmic losses in PEM electrolyzers and increasing performance—a trade-off that certainly needs to be re-evaluated when large-scale commercialization is considered.

Several studies have addressed this issue, successfully demonstrating an increased long-term OER performance for TiO_2-supported iridium oxides, exploiting viable synthesis methods that achieve conductive and stable OER anode materials.[14,26,27] These studies indicate that there is a beneficial relationship between the material's electrochemical OER activity and stability when mixing rather unstable but active iridium with stable but inactive TiO_2. However, only a few publications systematically explore the effects of deliberately tuned iridium−titanium composition on the material's OER activity−stability relationship, with studies mainly focusing on IrO_2 and TiO_2 mixtures.[28,−31]

Hence, this work systematically evaluates the OER activity, stability, and chemical as well as the electronic structure over a wide range of iridium−titanium ratios (Ir/[Ir + Ti]) by means of a thin film material library with an Ir-TiO_x compositional gradient (20−70 at. % Ir). A low-temperature (300 °C) heat treatment was used to gain insights into the benefits of intermixed iridium and substoichiometric TiO_x. Due to the unique nature of the sample preparation and the low annealing temperature, this study is focused on mixed Ir-TiO_x catalyst materials and screening their OER activity and stability over a wide composition range evaluated by means of a scanning flow cell (SFC) connected to an inductively coupled plasma mass spectrometer (ICP-MS).[32,33] Despite the limitation to low current densities, SFC-ICP-MS experiments provide meaningful insights for initial evaluation (and elimination) of material compositions[34,−36] prior to any long-term polarization studies at higher current densities,[37] facilitating catalyst development for PEM-WEs. In a recent similar study on a Ir-TiO_x composition gradient thin film material library, a nonlinear trend in iridium and titanium dissolution was observed.[31] However, no explanation was offered, stressing the demand for a more comprehensive study of the chemical and electronic properties of these Ir-TiO_x mixtures to elucidate the relationship between electronic properties and the OER activity and stability. To achieve this, complementary Ti $L_{2,3}$- and O K-edge X-ray absorption and depth-dependent X-ray photoelectron spectroscopy measurements were done to examine and quantify the chemical and electronic properties. Moreover, an online inductively coupled plasma mass spectrometer was used to simultaneously test the OER activity and stability of the set of mixed Ir-TiO_x catalyst candidate materials.

EXPERIMENTAL SECTION

Sample Preparation. The Ir-TiO_x thin film material library was prepared by using combinatorial magnetron sputtering[31] of Ir and Ti to create a compositional gradient of 20−70 at. % Ir (Ir−Ti ratio: Ir/[Ir + Ti]) across a length of 7 cm. The substrate was a 4 in. single-crystal Si (100) wafer with a 1.5 μm thermal SiO_2 barrier layer on top. The sputtering was performed in a high-vacuum magnetron sputter system (Bestec, Germany) equipped with 3 in. diameter Ir (99.9%, Evochem, Germany) and 3 in. diameter Ti (99.995%, FHR, Germany) targets. Prior to combinatorial sputtering, a uniform adhesion layer of 10 nm metallic Ti was deposited using a constant substrate rotation speed. Combinatorial sputtering of Ir and Ti to form a compositional gradient across the wafer was achieved by means of a static configuration and the confocal cathode arrangement of the targets. This resulted in a linear variation of the Ir−Ti ratio (20−70 at. % Ir) with position along the length of the substrate (see Figure 1). Complete details regarding the geometry of the sputtering setup and the SEM-EDX mapping characterization of the nominal Ir−Ti ratios achieved with this magnetron sputter system setup can be found in the Supporting Information of ref 31. The thickness of the deposited film is 200 nm. After sputter

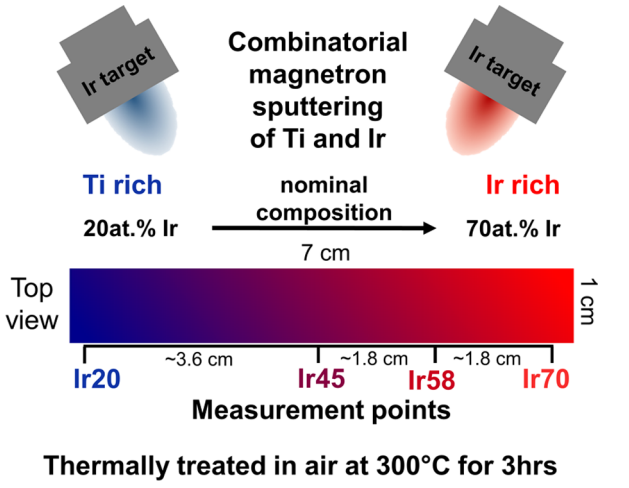

Figure 1. Compositional Ir-TiO_x material library schematic: preparation by combinatorial magnetron sputtering of Ti and Ir to create a Ir−Ti ratio composition range of 20−70 at. % Ir. Measurements were taken at four specific positions along the combinatorial sample, named samples Ir20, Ir45, Ir58, and Ir70 (indicating Ir−Ti ratios of 20, 45, 58, and 70 at. % Ir, respectively) in this study.

https://doi.org/10.1021/acscatal.3c02948
ACS Catal. 2023, 13, 15427−15438

deposition, the film was removed from UHV into ambient air and then thermally oxidized at 300 °C for 3 h, resulting in the compositional Ir-TiO_x material library.

All subsequent measurements were performed at four specific positions along the Ir-TiO_x thin film material library, representing the different Ir−Ti ratios chosen within the sample. These Ir−Ti ratios are hereafter named as samples Ir20, Ir45, Ir58, and Ir70, which represent different nominal Ir−Ti ratios (20, 45, 58, and 70 at. % Ir, respectively) of the material library as previously characterized by the SEM-EDX mapping done in ref 31.

Oxygen Evolution Reaction Activity and Stability. A scanning flow cell (SFC) connected to an inductively coupled plasma mass spectrometer (ICP-MS, NexION 350X, PerkinElmer) setup[9,32,33] was used to determine the OER activity and stability of the compositional Ir-TiO_x material library at each of the Ir−Ti ratios (samples Ir20, Ir45, Ir58, and Ir70). The geometric area of the measurement position is 0.01 cm^2, which is the opening of the V-shaped SFC. All measurements were performed using a 0.1 M $HClO_4$ solution as an electrolyte. The concentration of the dissolved titanium and iridium was determined by measuring intensities of ^{48}Ti and ^{193}Ir isotopes using online ICP-MS within the argon-saturated electrolyte pumped from the channels of the SFC. All potentials quoted are with respect to the reversible hydrogen electrode (RHE), which was determined before each measurement.

The electrochemical protocol (EP) follows a sequence of activity and stability measurements. Figures S1−S4 depict the EP steps (top plots) and corresponding measured dissolution rates of Ir and Ti (bottom plots) for samples Ir20, Ir45, Ir58, and Ir70. First, an activation of the working electrode at E = 1.2 V_{RHE} for 2 min (1. CA), followed by an anodic Linear Potential Sweep (LSV) at 10 mV/s from E = 1.2 V_{RHE} to a potential corresponding to a current density of j = 5 mA/cm^2 to describe the electrode's initial OER activity (2. LSV). Next is a chronopotentiometry (CP) hold at a current density of 1 mA/cm^2 for 2 min to track the electrode's time-resolved stability under the OER conditions (3. CP). Lastly, the electrode is subjected to a repeated anodic LSV at 10 mV/s from E = 1.2 V_{RHE} to a potential corresponding to a current density of j = 5 mA/cm^2 to characterize the change in the OER activity after a period of operation (4. repeated LSV).

The potential of the working electrode (E_{WE}, i.e., the potential of the Ir-TiO_x sample) required for reaching a current density of 5 mA/cm^2 is used as an OER activity descriptor here, facilitating comparison to other SFC-ICP-MS studies of thin film electrodes,[6,7,32,33,38,−43] hereafter referred to as "E_{WE} at j = 5 mA/cm^2". SFC-ICP-MS experiments are limited to operation at lower current densities due to gas bubble formation management issues. Typically for OER activity comparisons, anodic polarization curves are plotted (as seen in Figure 2a). For a more straightforward comparison, the E_{WE} at j = 5 mA/cm^2, obtained during the LSVs (EP steps 2. and 4.), is plotted as a function of the Ir−Ti ratio as seen in Figure 2b. A sputter deposited metallic iridium thin film (Ir_{ref}) is used as an internal benchmark for an iridium concentration of 100%.

To determine the total dissolved quantity of iridium and titanium normalized to the geometric area (ng/cm^2) for each EP step (the OER stability descriptor), the total area under the dissolution curves was integrated. Lastly, it is important to note that this setup provides information about initial dissolution rates of the catalyst. Different testing setup and protocol are required for addressing the effects of any long-term operation at higher current densities, closer to real-world conditions of PEM-WEs[37]. The scope of this study is limited to the initial screening of different Ir−Ti ratios (20−70 at. % Ir).

Synchrotron-Based X-Ray Absorption and X-Ray Photoelectron Spectroscopy Measurements. X-Ray absorption (XAS) measurements at the Ti $L_{2,3}$- and O K-edges were performed at Beamline 8.0.1. of the Advanced Light Source (ALS), Lawrence Berkeley National Laboratory, USA. The XAS measurements were performed at the iRIXS endstation equipped with a high-resolution variable line spacing soft X-ray spectrometer.[44] The XAS spectra were measured in surface-sensitive total electron yield (TEY) mode using the sample current and bulk-sensitive total fluorescence yield (TFY) mode utilizing the spectrometer and normalized by the incident photon flux, which was measured on a clean gold mesh placed upstream. The excitation energy was calibrated by measuring the Ti $L_{2,3}$- and O K-edge XAS spectra of a TiO_2 anatase (≥99.9% Sigma-Aldrich) and rutile (≥99.9% Sigma-Aldrich) as standard references (see Figure 3 and Figure S6, respectively). Angle-resolved Ti $L_{2,3}$ XAS was also performed to further elucidate differences in the titanium surface and bulk states (to test and exclude any significant self-absorption effects).

For the depth-dependent studies of the chemical and electronic structures of the compositional Ir-TiO_x material library at each of the Ir−Ti ratios (Ir20, Ir45, Ir58, and Ir70), soft X-ray (XPS) and hard X-ray (HAXPES) photoelectron spectroscopy were performed. This results in a range of different photoelectron inelastic mean free paths (IMFP) between 1.9 and 7.2 nm for photon energies of 1.45 and 5.95 keV. This is based on the calculations of the average IMFP for the different Ir−Ti ratios (20−70 at. %) in the mixed Ir-TiO_x thin film material library based on the IMFPs of the pure compounds,[45] see the Supporting Information for calculation details. The IMFP of metallic iridium is smaller than that of titanium and its oxides, due to its higher atomic density as determined by the TPP2M formula[46] using the QUASES software,[47] see Table S4. The average IMFP for the surface-sensitive XPS spectra ($IMFP_{1.45\ keV}$) thus ranges from 2.5 to 1.9 nm and for the bulk-sensitive HAXPES ($IMFP_{5.95\ keV}$) from 7.2 to 5.5 nm with increasing iridium content, see Table S5. The surface-sensitive 1.45 keV XPS measurements were performed at the SISSY I endstation (base pressure <10^{-8} mbar) located at the UE48 soft X-ray branchline (beam spot of 100 × 20 μm^2) of the EMIL two-color beamline, BESSY II, using a Scienta EW4000 electron energy analyzer. The bulk-sensitive HAXPES measurements at 5.95 keV were performed at the BL15XU beamline[48] (base pressure <10^{-7}mbar, beam spot of 25 × 35 μm^2) at SPring-8, with a Scienta R4000 electron energy analyzer. The binding energies (BE) for the XPS and HAXPES measurements were calibrated by adjusting the Au $4f_{7/2}$ BE of a clean gold foil to 84.00 eV.[49] The energy resolution values of the XPS and HAXPES measurements are 0.71 and 0.25 eV, respectively; see the Supporting Information for details. The geometry of the measurement setups and the photon energies of the two different beamlines were considered to estimate the (different) photoionization cross sections for quantitative analyses (calculations performed using SESSA[50]). All the expected Ir, Ti, and O and some trace C (presumably from surface adsorbates) related photoemission peaks are present in the survey spectra (Figures S8 and S9).

https://doi.org/10.1021/acscatal.3c02948
ACS Catal. 2023, 13, 15427−15438

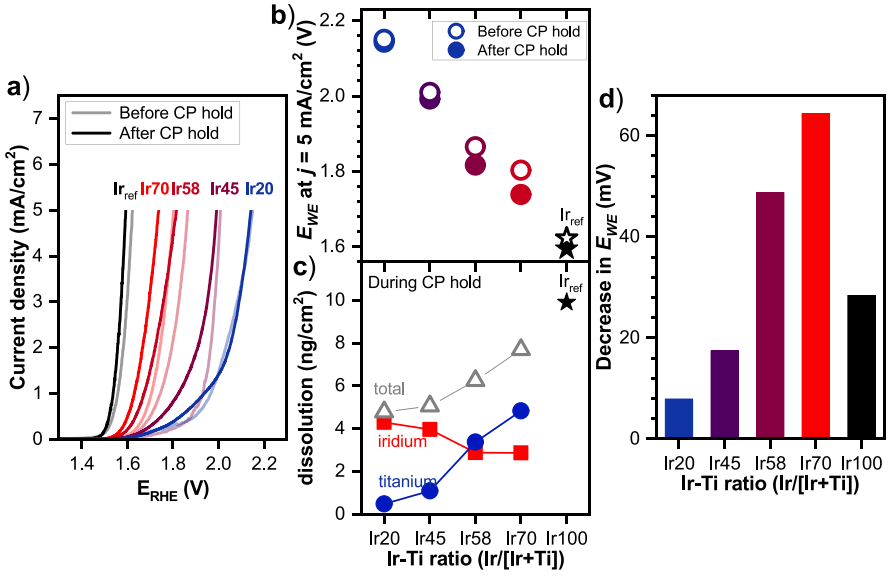

Figure 2. (a) Anodic polarization curves from 1.2 V_{RHE} to E_{WE} at j = 5 mA/cm^2 recorded with a scan rate of 10 mV/s (EP step 2. and EP step 4. before and after CP hold) for samples Ir20, Ir45, Ir58, and Ir70 of the compositional Ir-TiOx material library. The reference measurement on a sputter deposited metallic Ir thin film (Ir_{ref} = Ir100) used as an internal benchmark for an iridium concentration of 100% is shown in black. (b) OER activity represented by E_{WE} at j = 5 mA/cm^2 during the LSVs for the compositional Ir-TiO_x material library. The open circles correspond to LSVs before the CP hold (EP step 2.), and the filled circles correspond to LSVs after the CP hold (EP step 4.). The reference measurements on Ir_{ref} are shown in black stars. (c) OER stability obtained from the iridium and titanium dissolution quantities (and their totals = iridium + titanium) obtained during the CP hold at 1 mA/cm^2 for 2 min (EP step 3.) for the compositional Ir-TiO_x material library. The reference measurements on Ir_{ref} are shown in black stars. (d) OER activity improvement shown as the change (decrease) in the E_{WE} at j = 5 mA/cm^2 value after the CP hold at 1 mA/cm^2 for 2 min (EP step 3.) for the compositional Ir-TiO_x material library. The reference measurement on Ir_{ref} is shown in black. All measurements were performed in 0.1 M $HClO_4$.

Quantification of the Core-Level XPS and HAXPES Spectra. To quantify the depth-dependent Ir−Ti ratios from the XPS and HAXPES measurements, the peak areas of the overlapping asymmetric Ir 4f and symmetric Ir $5p_{1/2}$ and Ti 3s core-levels were fitted with asymmetric Finite Lorentzian[51] and Voigt profiles, respectively. For this shallow core-level region, the kinetic energies of the photoelectrons are very similar, and therefore, the core-level intensities were only corrected for the different photoionization cross sections[52,53] (given the different geometries and photon energies) and IMFPs[47] (average $IMFP_{1.45\ keV}$ and $IMPF_{5.95\ keV}$ for each Ir−Ti ratio), whereas the analyzer transmission function is negligible. Furthermore, similar photoelectron kinetic energies ensure that the presence of any surface adsorbates or contaminants affects the core-level intensities similarly.

To accurately determine the contribution of the Ir $5p_{1/2}$ and Ti 3s core-levels, which are overlapped by the prominent Ir 4f peaks, the Ir $5p_{3/2}$ and Ti 3p core-levels were also fitted. By constraining the peak areas of the Ir $5p_{1/2}$ and Ti 3s core-levels via their different photoionization cross section ratios with the peak areas of the Ir $5p_{3/2}$ and Ti 3p core-levels, the Ir−Ti ratios can be obtained from the overlapping Ir 4f, Ir $5p_{1/2}$, and Ti 3s core-level regions despite being dominated by the Ir 4f lines. Especially for samples with low Ti contents, it is crucially required to relate the fit of the Ti 3s core-level to the Ti 3p peak for which there is no overlap. Since the Ti 2p core-level is the most prominent in intensity and exhibits the narrowest lifetime broadening, the Ti 2p core-level spectra are used to identify the presence of different titanium species, i.e., Ti(IV), Ti(III), Ti(II), and Ti(0). Note that the Ti $2p_{3/2}$ and $2p_{1/2}$ core-levels display different Full-Width-Half-Maxima (FWHM) because of the presence of a Coster−Kronig decay[54] broadening the $2p_{1/2}$ core-level. Nevertheless, the doublet peak area ratio was kept constant according to $\frac{1+2l+1/2}{1+2l-1/2}$[49,55] while allowing the FWHM of the $2p_{3/2}$ and $2p_{1/2}$ to vary. The Ti 2p fit-derived information on the presence of the different titanium species is then used as a constraint to fit the respective spectral contributions of the Ti 3p and Ti 3s core-levels. The XPS spectra were fitted using the nonlinear optimization LMFIT package to dynamically generate the Shirley background and simultaneously fit identical core-levels for each excitation energy.[56] For further details on the LMFIT package and fitting parameters of the core-levels, see the Supporting Information. For a more general description of the degree of oxidation of the titanium species, an average TiO_x (where $0 < x \leq 2$) stoichiometry was calculated from the Ti(IV), Ti(III), and Ti(II) fit contributions of the Ti 2p spectra and is given as annotations in Figure 4d,e and tabulated in Table S3. See the Supporting Information for more details regarding these calculations.

RESULTS AND DISCUSSION

OER Activity and Stability of the compositional Ir-TiO_x material library. The activity−stability trends for the annealed compositional Ir-TiO_x material library are summarized in Figure 2. Figure 2a depicts the anodic polarization curves and subsequent derived activity of selected catalyst compositions (samples Ir20, Ir45, Ir58, and Ir70) as E_{WE} at j = 5 mA/cm^2 (Figure 2b). Figure 2c depicts the dissolution quantities of iridium and titanium, used as the metric for the OER stability. The lower the E_{WE} at j = 5 mA/cm^2, the higher the OER activity of the Ir-TiO_x candidate material.

The E_{WE} at j = 5 mA/cm^2 decreases by about 400 mV with an increasing iridium content (Ir20 → Ir70). The Ir70 sample

https://doi.org/10.1021/acscatal.3c02948
ACS Catal. 2023, 13, 15427−15438

displays the lowest E_{WE} at j = 5 mA/cm^2 (1.74 V_{RHE}) and the closest activity to that of the highly active Ir_{ref} (1.59 V_{RHE}), which agrees well with previous studies.[6,31] As iridium is the only electrochemically active material in the compositional Ir-TiO_x material library, it is considered to be solely responsible for the OER activity at the different Ir−Ti ratios. Increasing the amount of inactive titanium would decrease the number of iridium active sites, resulting in poorer OER activity. Therefore, the OER activity of the Ir-TiO_x samples increases as the iridium content increases (Ir20 → Ir70), which is in agreement with literature.[28,−31] Furthermore, there is a decrease in the E_{WE} at j = 5 mA/cm^2 potential before and after the CP hold at 1 mA/cm^2 (EP step 3.) indicating some increase in OER activity of the material (see the difference in the open and closed circles in Figure 2b and the E_{WE} at j = 5 mA/cm^2 improvement value in Figure 2d for each Ir−Ti ratio). This improvement (i.e., decrease) in E_{WE} at j = 5 mA/cm^2 is 8, 18, 49, and 64 mV for the samples Ir20, Ir45, Ir58, and Ir70, respectively.

Opposite trends in iridium and titanium dissolution are observed for the CP hold at 1 mA/cm^2: titanium dissolution, in blue, increases while iridium dissolution, in red, decreases with increasing Ir content (Ir20 → Ir70), as seen in Figure 2c. With increasing iridium content, the number of active sites for the OER increases, and therefore, a lower E_{WE} is required to achieve j = 5 mA/cm^2 (see Figure 2b). Therefore, higher dissolution rates of iridium are expected for lower Ir−Ti ratios. At high anodic potentials, the dissolution of iridium has been strongly linked to be triggered by OER itself,[39,−41,43] and higher E_{WE} at j = 5 mA/cm^2 values reflect harsher OER conditions. In contrast, lower titanium dissolution rates are observed for higher E_{WE} values at j = 5 mA/cm^2 potentials. This reverse in the trend of the titanium dissolution quantities is more likely observed due to possible passivation of Ti at high anodic potentials. However, the degree of passivation is unknown. Moreover, the cross-trend in iridium and titanium dissolution indicates that there must be other factor(s) influencing the stability of the titanium and iridium in the Ir-TiO_x material system during OER.

It has been well established that the extent of iridium dissolution[5,−7,9,40,42] is strongly linked to its formal oxidation state, which is typically derived from *ex situ* and *in situ* XAS and XPS measurements.[57,−60] Metallic iridium demonstrates a higher activity compared to rutile IrO_2 (1.58 V vs 1.69 V at 5 mA/cm^2 derived using a similar SFC-ICP-MS setup).[5,31] However, this higher activity is also paired with a higher dissolution rate, which is linked to the suspected formation of a hydrous, amorphous iridium oxide species on the metallic iridium surface.[6,7,42] This hydrated, amorphous IrO_x is more active but less stable against dissolution compared to rutile IrO_2.[5,7,8] In contrast, only a few studies have investigated the underlying mechanism of titanium dissolution at OER conditions for mixed Ir−Ti and Ir on Ti-based supports materials.[31,38,61,62] Nevertheless in most cases, the electronic state of the titanium in such materials remains unknown, which is somewhat surprising considering that titanium oxides often have semiconducting or even insulating properties, which can endanger employment of such catalysts in a real electrolyzer. The chemical speciation of iridium and titanium electronic states would give deeper insights into the mechanisms dictating the stability−activity relationship of the OER for different mixed Ir−Ti ratios. For this purpose, we discuss the results of our complementary X-ray spectroscopic studies next. XAS and XPS/HAXPES are exploited to provide insights into the chemical and electronic states formed by mixing iridium and titanium.

Characterization of the Ti Species using XAS. Prior to the OER activity and stability measurements, the chemical state and electronic structure of the titanium and oxygen species in the Ir-TiO_x samples of the compositional Ir-TiO_x material library were investigated using Ti $L_{2,3}$- and O K-edge XAS. Figure 3 displays the TEY and TFY Ti $L_{2,3}$XAS spectra (solid and dashed lines, respectively) of the compositional Ir-TiO_x material library, compared to the anatase (gray) and rutile (black) TiO_2 reference spectra. For the O K-edge XAS spectra and related discussions, please refer to Figure S6.

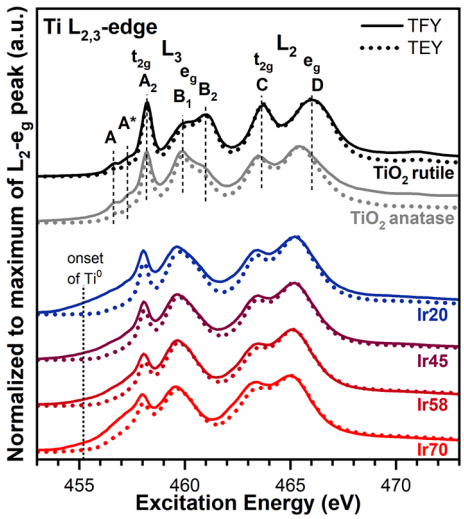

Figure 3. Ti $L_{2,3}$-edge XAS spectra of the Ir20, Ir45, Ir58, and Ir70 Ir-TiO_x samples collected in the TFY (solid lines) and TEY (dotted lines) modes compared to corresponding anatase and rutile TiO_2 reference spectra. The spectra are normalized to the L_2-e_g peak intensity.

The Ti $L_{2,3}$ absorption edge probes the transition of the occupied Ti 2p ($2p_{1/2}$ and $2p_{3/2}$) core-level into unoccupied Ti 3d-derived states. This results in well-known splitting of the final states (L_2 and L_3 peaks), with pre-edge features (A and A*) attributed to core-hole d-electron interactions.[63,64] Further resolution of the L_2 and L_3 peaks into t_{2g} and e_g peaks occurs due to crystal field splitting.[65,66] Additionally, the L_3-e_g peak further splits (B_1 and B_2) due to differences in tetragonal distortion of the TiO_6 octahedron, as prominently showcased in the TiO_2 anatase and rutile polymorph spectra[64,67] (gray and black spectra in Figure 3).

The TEY and TFY Ti $L_{2,3}$-edge XAS spectra of the compositional Ir-TiO_x material library exhibited strong differences when compared to the anatase and rutile TiO_2 references, including (1) a shift of the maximum L_3-t_{2g} peak toward lower excitation energies, (2) a broadening of the L_3-t_{2g} peak, (3) the appearance of a large absorption shoulder at lower excitation energies (453−457.5 eV), (4) less resolved L_3-e_g splitting, and (5) altered t_{2g}/e_g peak ratios. These observations suggest the presence of metallic Ti and an assortment of titanium-suboxides (TiO_x where x < 2)[67,−71] in the compositional Ir-TiO_x material library. The lower absorption edge of metallic Ti (indicated by the dashed vertical line in Figure 3), 3 eV lower than that of TiO_2, 458.2 eV,[68] accounts for the spectral intensity at lower excitation

https://doi.org/10.1021/acscatal.3c02948
ACS Catal. 2023, 13, 15427−15438

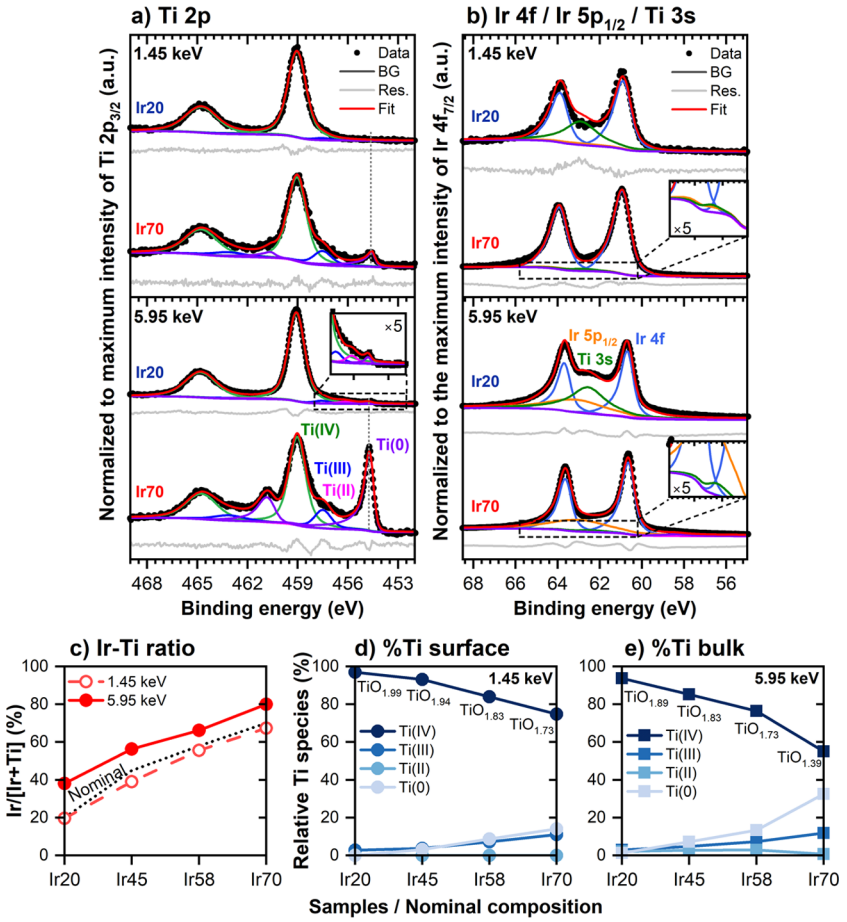

Figure 4. (a) Ti 2p spectra (including fits) and (b) overlapping Ir 4f/Ir $5p_{1/2}$/Ti 3s spectra (including fits) for samples Ir20 and Ir70 of the compositional Ir-TiO_x material library recorded with surface-sensitive 1.45 keV (top plots) and bulk-sensitive 5.95 keV (bottom plots) excitation energies. The raw data, fit curve (fit), background (BG), and fit residuals (residues) are shown. (c) Quantified surface and bulk-sensitive Ir/[Ir + Ti] ratio derived from the Ir 4f/Ir $5p_{1/2}$/Ti 3s fit, where Ir = Ir(0) and Ti = Ti(IV) + Ti(III) + Ti(II) + Ti(0), and the relative content of the titanium species (Ti(IV), Ti(III), Ti(II), and Ti(0)) identified in the surface-sensitive (1.45 keV, (d)) and bulk-sensitive (5.95 keV, (e)) measurements of the Ti 2p spectra. Annotated in panels d and e is the average TiO_x stoichiometry (where $0 < x < 2$) calculated from the Ti(IV), Ti(III), and Ti(II) fit contributions of the Ti 2p spectra.

energies. The other observations are well-known indications of substoichiometric titanium oxidation states,[67−71] reflecting an increased Ti 3d character in the absorption spectra with a decreasing titanium oxidation state.

These spectral differences become more pronounced with increasing iridium content (Ir20 → Ir70), indicating a growing deviation of the structure of the Ti oxide within the Ir-TiO_x samples from the anatase and rutile TiO_2 references. While these features become more pronounced with increasing iridium content, the overall similarity in the TEY and TFY Ti $L_{2,3}$-edge XAS spectral shape between the compositional Ir-TiO_x material library compared and TiO_2 suggests that the predominant Ti species in the studied Ir-TiO_x samples remains as TiO_2.

Furthermore, the difference in peak shapes and intensities of TEY and TFY Ti $L_{2,3}$-edge XAS indicates a strong difference between bulk and surface titanium states. Notably, the large absorption shoulder of the L_3-t_{2g} peak (453−457.5 eV) is less intense for the surface-sensitive TEY compared to the bulk-sensitive TFY measurements of the compositional Ir-TiO_x material library. The contrast between surface and bulk states is most evident in sample Ir20, where the surface predominantly exhibits TiO_2 character, while the bulk has a pronounced metallic Ti and TiO_x character. The difference between the surface and bulk spectra decreases with increasing Ir content, particularly from sample Ir20 to Ir45. In sample Ir70, the small difference between TFY and TEY, along with the overall high absorption intensity for the broad L_3-t_{2g} shoulder feature, suggests that both the surface and bulk states have more a metallic Ti and TiO_x character. To further elucidate the subtle difference between surface and bulk states in sample Ir70, angle-resolved TEY and TFY Ti $L_{2,3}$-edge XAS measurements were performed (see Figure S7). At more grazing angles (i.e., more surface-sensitive), the lower spectral intensity in the 453−457.5 eV energy regime indicates a more oxidized surface with minor amounts of metallic Ti and TiO_x. In conclusion, depending on the Ir−Ti ratio (20−70 at. % Ir), we find by Ti $L_{2,3}$ XAS (Figure 3 and Figure S7) Ti existing in varying chemical environments, predominantly described as TiO_2 (dominating the sample surface) and a combination of metallic Ti with an assortment of different TiO_x species (dominating the sample bulk).

Due to the varying concentrations of the TiO_2, metallic Ti, and TiO_x species (TiO_2−TiO_x-Ti^0 composition), and their differences in electrical conductivity, we anticipate significant differences in the conductivity of the compositional Ir-TiO_x

https://doi.org/10.1021/acscatal.3c02948
ACS Catal. 2023, 13, 15427−15438

material library for the different IrTi ratios compared to semiconductive TiO_2. Titanium suboxide Magnéli phases (Ti_nO_{2n-1})[9] and Ti_2O_3[10] are more electrically conductive than TiO_2. Therefore, an increased quantity of the TiO_x species and metallic Ti in the material is expected to enhance electrical conductivity, directly impacting the catalytic behavior of the material. This is supported by lower E_{WE} at j = 5 mA/cm^2 values (indicating better catalytic activity) for Ir−Ti ratios with higher TiO_x and Ti concentrations, while higher contributions of TiO_2 leads to a decreased conductivity and higher E_{WE} at j = 5 mA/cm^2 values (Figure 2b). Additionally, since there is also a depth-dependent TiO_2−TiO_x−Ti^0 composition gradient, we also anticipate a pronounced conductivity profile that changes from the surface to the bulk for each of the different Ir−Ti ratios.

This underscores the importance of quantifying and understanding the TiO_2−TiO_x−Ti^0 composition profile in the compositional Ir-TiO_x material library. Conventional techniques, such as four-point probe resistivity measurements, are not suitable for determining these electrical conductivity profiles. Furthermore, speciation and quantification of the Ti species are not straightforward using XAS. Reference measurements of every possible titanium oxide species (TiO_x for all possible $x < 2$) would be required to quantify the data by, e.g., principle component and linear combination analysis. A better approach is to use photoelectron spectroscopy for speciation and quantification, as it can also be used to gain depth-dependent information on the TiO_2−TiO_x−Ti^0 composition when different excitation energies are exploited. This information is expected to yield insights that explain the unexpected trend in the titanium dissolution and catalytic behavior of the Ir−Ti ratios. It has been shown for compact rutile IrO_2 thin films that the first ∼2.5 nm of the catalyst film is involved in the OER.[41] The bulk composition contributes toward the overall charge transport pathways within the material and hence can influence the overall OER performance of the material. Therefore, depth-dependent information provides an understanding of both the active surface layer and deeper charge transport layers within the material. Additional speciation of the iridium can shed light on the (partially) improved OER activity−stability relationship of thin film material library compared to Ir_{ref}, by establishing a link between stability and formal oxidation state.

Compositional Analysis by Depth-Resolved Photoelectron Spectroscopy. Excitation-energy-dependent (i.e., depth-dependent) photoelectron spectroscopy measurements were performed to clarify the chemical structure and composition at the surface (XPS: 1.45 keV) and in the bulk (HAXPES: 5.95 keV) of the Ir-TiO_x compositional material library, for each of the Ir−Ti ratio (20−70 at. % Ir), prior to OER activity and stability measurements. This information sheds light on the nature of the iridium and titanium species, dictating the OER activity and stability for each Ir−Ti ratio in the Ir-TiO_x compositional material library. The XPS and HAXPES survey spectra are shown in Figures S8 and S9. Figure 4a,b summarizes the Ti 2p and Ir 4f/Ir 5$p_{1/2}$/Ti 3s fits of the surface and bulk for sample Ir20 and Ir70 of the compositional Ir-TiO_x material library. The surface and bulk Ir−Ti ratios shown in Figure 4c and Figure 4d,e depict the surface and bulk content of the present Ti species, annotated with the average TiO_x stoichiometry (where $0 < x \leq 2$) calculated from the Ti(IV), Ti(III), and Ti(II) fit contributions of the Ti 2p spectra.

The surface-sensitive and bulk-sensitive measurements reveal the presence of a depth-dependent Ir−Ti ratio profile for each of the Ir−Ti ratios in the Ir-TiO_x compositional material library (Figure 4d). The more surface-sensitive (1.45 keV, average IMFP of 2.5−1.9 nm) data indicate on average 16% richer titanium composition compared to more bulk-sensitive (5.95 keV, average IMFP of 7.2−5.5 nm) measurement. The ratio of Ir−Ti directly affects the OER performance of the material through alterations in the concentration of the active species at the surface (i.e., Ir, as Ti is not OER active) and through charge transport properties, mostly dictated by the concentration and nature of the titanium species at the surface and in the bulk.

Regarding the active Ir species, no appreciable (detectable) amount of surface iridium oxide was observed (Figure 4b), as can be expected starting to form at 300 °C,[42] with a strong oxidation process forming rutile IrO_2 only reported for temperatures ≥400 °C.[42,72,73] The singular asymmetric Ir 4$f_{7/2}$ peak at a binding energy of 60.9 eV[57,58] indicates the presence of only Ir(0), irrespective of depth sensitivity. This can presumably be related to the higher oxygen affinity of titanium[74] compared to iridium.[75] At 300 °C, only the titanium species (not the iridium) is oxidized, which supports the initial evidence given by the Ti $L_{2,3}$- and O K-edge XAS measurements regarding the presence of a TiO_2−TiO_x-Ti^0 matrix. Therefore, metallic Ir (and its concentration at the surface) is solely responsible for the catalytic OER activity of different Ir−Ti ratios in the Ir-TiO_x compositional material library reported in Figure 2.

In accordance with the Ti $L_{2,3}$- and O K-edge XAS results, the analysis of the fitted Ti 2p spectra (Figure 4a,d,e) confirms the predominance of the Ti(IV) oxide (Ti 2$p_{3/2}$ position = 458.9 eV[49,76]) irrespective of iridium content, with a minimum amount of 58% (Ir70, 5.95 keV). Much lower concentrations of Ti(III)O_x and Ti(II)O_x suboxides are observed, with a maximum amount of 13% (Ir70, 5.95 keV). There is still an appreciable amount of metallic Ti(0) (Ti 2$p_{3/2}$ position = 454.5 eV) remaining after oxidation at 300 °C with a maximum contribution of 33% (Ir70, 5.95 keV). A strong variation in the TiO_2−TiO_x-Ti^0 compositions with the Ir−Ti ratios is observed in the Ir-TiO_x compositional material library. The concentrations of the TiO_x suboxides and metallic Ti increase with higher iridium concentrations, whereas lower Ir−Ti ratios show high proportions of TiO_2. Furthermore, the surface-sensitive XPS measurements (1.45 keV, average IMFP of 2.5−1.9 nm) indicate lower concentrations of TiO_x and metallic Ti, which is in accordance with the surface-sensitive Ti $L_{2,3}$ TEY. Also, the bulk-sensitive HAXPES measurements (5.95 keV, average IMFP of 7.2−5.5 nm) are in good agreement with the bulk-sensitive TFY-XAS measurements as they reveal a more stoichiometric TiO_2 surface layer. The average surface stoichiometry decreases from $TiO_{1.99}$ to $TiO_{1.73}$, while the average more bulk-sensitive stoichiometry decreases from $TiO_{1.89}$ to $TiO_{1.39}$ with increasing Ir−Ti ratios. It is therefore proposed that strong oxidation mainly occurs in the first few surface layers, and once this nearly stoichiometric surface oxide layer is formed, it creates an oxygen diffusion barrier limiting titanium oxidation in the bulk. Moreover, the lower degree of titanium oxidation with increasing iridium content suggests that the presence of iridium influences the oxidation process of titanium. Although iridium itself does not oxidize at the investigated low temperatures, its high concentrations may provide an additional physical barrier

https://doi.org/10.1021/acscatal.3c02948
ACS Catal. 2023, 13, 15427−15438

hindering oxygen diffusion within the film preventing oxygen from reacting with the titanium species. This is consistent with a previous study[31] reporting lower oxygen concentrations in deeper layers of the materials and no oxygen within iridium-rich grain regions.

Our XAS and XPS/HAXPES results collectively describe the composition of the Ir-TiO_x material library as a mixed metallic Ir, metallic Ti, and TiO_x ($0 < x \leq 2$) matrix, with variations in the extent of titanium oxidation depending on depth and iridium content. This variation likely leads to a variation in the conductivities within the compositional Ir-TiO_x material library, depending on the Ir−Ti ratios and depth within the film. This Ir^0-Ti^0-TiO_x composition (and its variation with depth) has a direct impact on the OER activity and stability of the material, which we discuss in the next section.

Effect of the Ir−Ti Ratio on OER Activity and Stability. Given the elucidation of the surface and bulk Ir^0-Ti^0-TiO_x composition by means of XAS and XPS/HAXPES, a deeper understanding of the trends in the OER activity and stability (as shown in Figure 2) can be gained.

Because of the low annealing temperature, the titanium exists in an intermixed matrix of semiconductive but stable TiO_2 together with more conductive, less stable TiO_x suboxides and highly conductive but highly unstable metallic Ti. As demonstrated by several studies, the use of substoichiometric titanium oxides as, e.g., Magnéli phases[17,18,23] can improve the charge transport pathways and hence the overall OER performance of the material. Therefore, using a low annealing temperature of 300 °C results in the beneficial formation of a more conductive assortment of TiO_x species, which is expected to improve the electrical conductivity within the material. In contrast, the material's stability against dissolution is reduced. According to the Pourbaix diagram, under OER potentials in acidic media, TiO_2 and TiO are the most thermodynamically favored species,[25] and therefore, Ti and Ti(III)O_x oxides are expected to undergo phase transitions leading to higher dissolution rates. The unusual trend in titanium dissolution as shown in Figure 2c can therefore be correlated with the change in titanium species composition. For low iridium content, the titanium species at the sample surface is predominantly in a near-stoichiometric state ($TiO_{1.99}$) that is very stable under the OER conditions. With increasing iridium content, increased amounts of metallic Ti and TiO_x form, up to 3% metallic Ti and 11% $TiO_{1.73}$ (see Figure 4d,e), which are less stable in the harsh acidic OER conditions. Therefore, with increasing iridium content and corresponding lower overpotentials, higher dissolution rates of titanium are observed due to the presence of a larger quantity of less stable Ti^0 and Ti(III) oxide within the electrode. This explains the reverse trend in titanium dissolution compared with iridium dissolution.

Despite the increase in the titanium dissolution rates with increasing Ir−Ti ratios, under the OER conditions of the CP hold at 1 mA/cm^2 for 2 min, all Ir−Ti ratios in the compositional Ir-TiO_x material library display higher stability against iridium dissolution compared to Ir_{ref}. Figure 5 presents the overall quantified Ir(0), Ti(IV), Ti(III), Ti(II), and Ti(0) surface and bulk compositions, along with the relative iridium stability presented on the secondary *y*-axis, which is the iridium dissolution quantity of the Ir-TiO_x samples (d_{Ir-TiO_x}) with respect to the iridium dissolution quantity of Ir_{ref} ($d_{Ir_{ref}}$) during the CP hold at 1 mA/cm^2 for 2 min. The larger this value is,

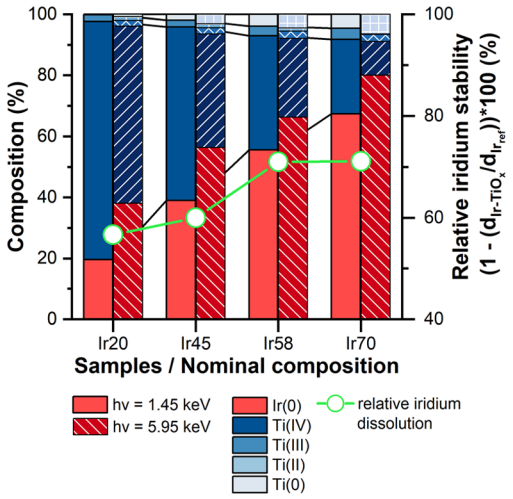

Figure 5. Ir(0), Ti(IV), Ti(III), Ti(II), and Ti(0) composition derived by means of surface (XPS 1.45 keV) and bulk (HAXPES: 5.95 keV) sensitive measurements for samples Ir20, Ir45, Ir58, and Ir70 of the studied compositional Ir-TiO_x material library. Given on the secondary *y*-axis (right) is the relative iridium sample stability with respect to the Ir_{ref}. Here, the relative stability represents the ratio of the iridium dissolution quantity of the Ir-TiO_x samples (d_{Ir-TiO_x}) and the iridium dissolution of Ir_{ref} ($d_{Ir_{ref}}$) for the EP step CP hold at 1 mA/cm^2 for 2 min.

the lower the iridium dissolution for that specific mixed Ir-TiO_x catalyst candidate material composition. The lowest iridium dissolution (i.e., highest relative iridium stability) was observed for samples Ir58 and Ir70. This demonstrates that even a small quantity of intermixed titanium stabilizes the iridium species against dissolution, despite the titanium species itself being less stable against dissolution. For the compositions with the lowest iridium dissolution, higher concentrations of metallic Ti and TiO_x compared to stoichiometric TiO_2 are observed. The counter advantage of having a titanium species in a less stable state (i.e., TiO_x vs TiO_2) is that it has better conductivity, which contributes to the increased performance of the material (as can be seen by low E_{WE} at j = 5 mA/cm^2 value in Figure 2b). Furthermore, the higher quantities of conductive species (i.e., Ir(0), Ti(0), Ti(III), and Ti(II)) in the bulk better promote charge transport pathways within the material for PEM-WE application needs.

The other interesting result from this study is that there is an overall reduction in the total dissolution amounts of iridium and titanium (Figure S5 for the dissolution rates for each EP step) and a simultaneous improvement in OER activity before and after the CP hold at 1 mA/cm^2 (see Figure 2d). The total dissolution of iridium and titanium decreases in average by 63 and 89%, respectively, after the EP protocol, indicating rapid stabilization of the electrode surface. Simultaneously, the lower E_{WE} at j = 5 mA/cm^2 observed after the CP hold at 1 mA/cm^2 implies that an activation process has occurred on the surface of the material. The extent of these activation and stabilization processes increases with increasing Ir−Ti ratio. It is well-known that, for metallic iridium, there is an initial activation of the surface through the formation of a highly active hydrous iridium oxide species,[6,7] which leads to the observed decrease of 28 mV in the E_{WE} at j = 5 mA/cm^2 before and after the CP hold at 1 mA/cm^2 for the Ir_{ref} benchmark. It is quite probable that the compositional Ir-TiO_x material library also undergoes

https://doi.org/10.1021/acscatal.3c02948
ACS Catal. 2023, 13, 15427−15438

a similar activation of its metallic iridium species. However, for some of the Ir−Ti ratios in the material library, the reduction in E_{WE} at j = 5 mA/cm^2 is much larger than that of the metallic iridium benchmark (e.g., 49 mV for Ir58 and 64 mV for Ir70, see Figure 2d). This leads to the conclusion that there are other additional processes occurring that improve the material's OER activity for these samples. One possible explanation is the more rapid dissolution of the surface metallic Ti, which is less stable compared to nearly stoichiometric TiO_x, and this preferential dissolution of metallic Ti can create microporosity within the surface layer, leaving behind a more stable (TiO_x vs metallic Ti) and more active material (i.e., more exposed Ir sites). This could explain why the extent of activation (i.e., the decrease in E_{WE} at j = 5 mA/cm^2 of 64 mV) is the highest for sample Ir70 (see Figure 2d), which has the highest Ti^0 (3.5%) and $TiO_{1.73}$ (29.2%) quantities. This phenomenon has also been observed for nonstoichiometric $Ir_{0.7}Sn_{0.3}O_{2-x}$ thin films, which showed improved OER activity as a result of the preferential dissolution of less stable, nonstoichiometric $Sn_{0.3}O_{2-x}$ compared to the iridium, resulting in a porous structure with an activated hydrous iridium surface.[34]

Using a rather low annealing temperature, an optimal mixture of highly stable TiO_2 with an assortment of more conductive and less stable TiO_x and metallic Ti can be formed for a wide range of Ir−Ti ratios. This has a direct effect on the OER activity and stability for each of the Ir−Ti ratios. The best-performing Ir−Ti samples investigated within this study are Ir58 and Ir70, for which moderate, beneficial amounts of metallic Ti and TiO_x improve the material's OER activity and stability against iridium dissolution compared to the Ir_{ref}. This study strongly highlights the beneficial nature of mixing conductive, but less stable, titanium-suboxides with iridium. First, the intermixed titanium promotes stabilization of the iridium species in the Ir-TiO_x candidate materials. Second, there is an initial increase in OER performance by an increase in the available iridium active sites via selective dissolution of the comparatively less stable titanium species, leading to increased surface porosity. Lastly, there is increased conductivity of the mixed Ir-TiO_x catalyst by the formation of conductive titanium-suboxides. The previous findings[31] alone are insufficient to explain these three effects. The use of XAS and XPS/HAXPES therefore allowed for a deeper understanding of the electronic states of iridium and titanium governing the material's OER activity and stability and provided a better insight into the conductivity (e.g., charge transport pathways) of the material.

Long-term stability of these material compositions is yet to be proven; still, the insights on the initial titanium and iridium dissolution rates presented here provide a good basis for stability comparison of catalysts with different Ir−Ti compositions. Ref 31 reported that such mixed Ir-TiO_x thin film materials displayed higher S-numbers (i.e., higher stability) compared to thermally formed rutile IrO_2 and IrO_2/TiO_2 nanoparticles.[62] It has also been shown that aqueous model systems are ideal for studying beginning of life accelerated stability tests, comparable to dissolution rates in membrane electrode assemblies, reflecting PEM-WE performance.[37] Therefore, the information on the thin film compositional Ir-TiO_x material presented in this study can be used for the rational design of active and stable OER catalysts with low Ir loading.

CONCLUSIONS

A systematic evaluation of the OER activity and stability of a wide range of Ir−Ti ratios (20−70 at. % Ir) by means of a thin film compositional Ir-TiO_x material library was performed. Synchrotron Ti $L_{2,3}$-edge and O K-edge XAS and depth-dependent XPS/HAXPES measurements revealed that, using a low annealing temperature of 300 °C, the formation of an intermixed metallic Ir^0, Ti^0, TiO_2, and assorted TiO_x (x < 2) suboxide matrix is achieved. The extent of titanium oxidation depends strongly on the iridium content and sample depth, with high ratios of Ti^0 and TiO_x observed at the highest iridium concentrations and in the surface region of the studied samples. The intermixed matrix of semiconductive but stable TiO_2, more conductive TiO_x suboxides, and highly conductive metallic Ti yielded improved stability against iridium dissolution compared to a metallic iridium thin film benchmark. In addition, it also improved OER activity by means of better electrical conductivity and preferential dissolution of the nonstoichiometric titanium oxides and metallic titanium to create more exposed iridium active sites.

By means of a co-sputtered material library, we demonstrated the ability to tune the Ir−Ti ratio, allowing for efficient screening of the OER catalyst materials. Changes in morphologies and chemical states were directly linked with OER stability and activity of the OER and the material's conductivity. This approach elucidated viable (well-performing) Ir/Ti ratios suitable for further catalyst development strategies with the aim of reducing iridium loading. This knowledge can aid in tailoring more stable mixed Ir-TiO_x catalysts with lower Ir loading for OER applications and highlights the beneficial impact of the different titanium phases that are formed using low annealing temperatures.

ASSOCIATED CONTENT

Supporting Information

The Supporting Information is available free of charge at https://pubs.acs.org/doi/10.1021/acscatal.3c02948.

Additional electrochemical activity and stability measurement details and results; O K-edge XAS results; angle-resolved Ti $L_{2,3}$-edge XAS results; XPS and HAXPES survey spectra; XPS and HAXPES energy resolution calculations; Ti 2p and Ir 4f/Ir 5p/Ti 3s/Ti 3p XPS and HAXPES spectra, fitting logic and line shape parameters; and average IMFP calculations (PDF)

AUTHOR INFORMATION

Corresponding Authors

Marianne van der Merwe − *Interface Design, Helmholtz Zentrum Berlin für Materialien und Energie GmbH, Berlin 12489, Germany;* orcid.org/0000-0002-3182-1392; Email: marianne.vdm@helmholtz-berlin.de

Marcus Bär − *Interface Design, Helmholtz Zentrum Berlin für Materialien und Energie GmbH, Berlin 12489, Germany; Energy Materials In-Situ Laboratory Berlin (EMIL), Helmholtz Zentrum Berlin für Materialien und Energie GmbH, Berlin 12489, Germany; Department of Chemistry and Pharmacy, Friedrich-Alexander-Universität ErlangenNürnberg, Erlangen 91058, Germany; X-Ray Spectroscopy at Interfaces of Thin Films, HI ERN, Berlin 12489, Germany;* orcid.org/0000-0001-8581-0691; Email: marcus.baer@helmholtz-berlin.de

https://doi.org/10.1021/acscatal.3c02948
ACS Catal. 2023, 13, 15427−15438

Authors

Raul Garcia-Diez − *Interface Design, Helmholtz Zentrum Berlin für Materialien und Energie GmbH, Berlin 12489, Germany;* orcid.org/0009-0000-9374-1083

Leopold Lahn − *Dynamic Electrocatalytic Interfaces, Helmholtz Zentrum Berlin für Materialien und Energie GmbH, Berlin 14109, Germany; Helmholtz-Institute Erlangen-Nürnberg for Renewable Energy (HI ERN), Erlangen 91058, Germany; Department of Materials Science and Engineering, Friedrich-Alexander-Universität ErlangenNürnberg, Erlangen 91058, Germany*

R. Enggar Wibowo − *Interface Design, Helmholtz Zentrum Berlin für Materialien und Energie GmbH, Berlin 12489, Germany;* orcid.org/0000-0002-8325-0413

Johannes Frisch − *Interface Design, Helmholtz Zentrum Berlin für Materialien und Energie GmbH, Berlin 12489, Germany*

Mihaela Gorgoi − *Interface Design, Helmholtz Zentrum Berlin für Materialien und Energie GmbH, Berlin 12489, Germany; Energy Materials In-Situ Laboratory Berlin (EMIL), Helmholtz Zentrum Berlin für Materialien und Energie GmbH, Berlin 12489, Germany*

Wanli Yang − *Advanced Light Source (ALS), Lawrence Berkeley National Laboratory, Berkeley, California 94720, United States;* orcid.org/0000-0003-0666-8063

Shigenori Ueda − *Synchrotron X-ray Station at SPring-8, National Institute for Materials Science (NIMS), Sayo, Hyogo 679-5148, Japan; Research Center for Electronic and Optical Materials, NIMS, Ibaraki 305-0044, Japan*

Regan G. Wilks − *Interface Design, Helmholtz Zentrum Berlin für Materialien und Energie GmbH, Berlin 12489, Germany; Department of Materials Science and Engineering, Friedrich-Alexander-Universität ErlangenNürnberg, Erlangen 91058, Germany;* orcid.org/0000-0001-5822-8399

Olga Kasian − *Dynamic Electrocatalytic Interfaces, Helmholtz Zentrum Berlin für Materialien und Energie GmbH, Berlin 14109, Germany; Helmholtz-Institute Erlangen-Nürnberg for Renewable Energy (HI ERN), Erlangen 91058, Germany; Department of Materials Science and Engineering, Friedrich-Alexander-Universität ErlangenNürnberg, Erlangen 91058, Germany;* orcid.org/0000-0001-6315-0637

Complete contact information is available at: https://pubs.acs.org/10.1021/acscatal.3c02948

Author Contributions

M.v.d.M. and R.G.D. conceptualized the project. M.v.d.M. carried out most of the characterizations, analyzed and interpreted all of the data, and prepared the manuscript. L.L. and O.K. carried out the SFC-ICP-MS measurements and provided support in the data evaluation. R.G.W. performed the HAXPES measurements. M.v.d.M. and J.F. performed the XPS measurements. M.v.d.M., R.E.W., R.G.D., R.G.W., and M.B. performed the XAS measurements. W.L. provided support for measurements at ALS beamline 8.0.1. M.G. provided support for measurements at beamline UE48 at EMIL, HZB. S.U. provided support for measurements at beamline BL15XU at SPring-8. All authors contributed to the scientific discussion of the results and manuscript draft preparation and had approved the final version of the manuscript.

Notes

The authors declare no competing financial interest.

ACKNOWLEDGMENTS

This work was partially funded by the German Federal Ministry of Education and Research (BMBF) in the framework of the Kopernikus P2X project (ID: 03SFK2X0-2) and by the Impuls- and Vernetzungsfonds of the Helmholtz-Association (VH-NG-423). R.G.D. acknowledges funding by the German Federal Ministry of Education and Research in the framework of the CatLab project (03EW0015A/B). O.K. acknowledges funding from the German Research Foundation (DFG), Project-ID 431791331 − SFB 1452. The authors are grateful to the Energy Materials In-Situ Laboratory (EMIL) BESSY II and the NIMS Synchrotron X-Ray Station at SPring-8 for providing access to beamtime for XPS and HAXPES measurements (proposal no.: 2019B4910). This research used resources of the Advanced Light Source, which is a DOE Office of Science User Facility under contract no. DE-AC02-05CH11231. The authors thank Andrea M. Mingers at the Max-Planck-Institut für Eisenforschung GmbH for support with the SFC-ICP-MS measurements. Thanks are also extended to Dr. Wilson Quevedo for proof reading, discussion, and positive feedback on this work.

REFERENCES

(1) Carmo, M.; Fritz, D. L.; Mergel, J.; Stolten, D. A Comprehensive Review on PEM Water Electrolysis. *Int. J. Hydrogen Energy* **2013**, *38* (12), 4901−4934.

(2) Buttler, A.; Spliethoff, H. Current Status of Water Electrolysis for Energy Storage, Grid Balancing and Sector Coupling via Power-to-Gas and Power-to-Liquids: A Review. *Renew. Sustain. Energy Rev.* **2018**, *82*, 2440−2454.

(3) Schlögl, R. The Role of Chemistry in the Energy Challenge. *ChemSusChem* **2010**, *3* (2), 209−222.

(4) Schalenbach, M.; Tjarks, G.; Carmo, M.; Lueke, W.; Mueller, M.; Stolten, D. Acidic or Alkaline? Towards a New Perspective on the Efficiency of Water Electrolysis. *J. Electrochem. Soc.* **2016**, *163* (11), F3197−F3208.

(5) Cherevko, S.; Geiger, S.; Kasian, O.; Kulyk, N.; Grote, J.-P.; Savan, A.; Shrestha, B. R.; Merzlikin, S.; Breitbach, B.; Ludwig, A.; Mayrhofer, K. J. J. Oxygen and Hydrogen Evolution Reactions on Ru, RuO_2, Ir, and IrO_2 Thin Film Electrodes in Acidic and Alkaline Electrolytes: A Comparative Study on Activity and Stability. *Catal. Today* **2016**, *262*, 170−180.

(6) Cherevko, S.; Geiger, S.; Kasian, O.; Mingers, A.; Mayrhofer, K. J. J. Oxygen Evolution Activity and Stability of Iridium in Acidic Media. Part 1. - Metallic Iridium. *J. Electroanal. Chem.* **2016**, *773*, 69−78.

(7) Cherevko, S.; Geiger, S.; Kasian, O.; Mingers, A.; Mayrhofer, K. J. J. Oxygen Evolution Activity and Stability of Iridium in Acidic Media. Part 2. - Electrochemically Grown Hydrous Iridium Oxide. *J. Electroanal. Chem.* **2016**, *774*, 102−110.

(8) Jovanovič, P.; Hodnik, N.; Ruiz-Zepeda, F.; Arčon, I.; Jozinović, B.; Zorko, M.; Bele, M.; Šala, M.; Šelih, V. S.; Hočevar, S.; Gaberšček, M. Electrochemical Dissolution of Iridium and Iridium Oxide Particles in Acidic Media: Transmission Electron Microscopy, Electrochemical Flow Cell Coupled to Inductively Coupled Plasma Mass Spectrometry, and X-Ray Absorption Spectroscopy Study. *J. Am. Chem. Soc.* **2017**, *139* (36), 12837−12846.

(9) Kasian, O.; Geiger, S.; Mayrhofer, K. J. J.; Cherevko, S. Electrochemical On-Line ICP-MS in Electrocatalysis Research. *Chem. Rec.* **2019**, *19* (10), 2130−2142.

(10) Cherevko, S.; Zeradjanin, A. R.; Topalov, A. A.; Kulyk, N.; Katsounaros, I.; Mayrhofer, K. J. J. Dissolution of Noble Metals during Oxygen Evolution in Acidic Media. *ChemCatChem.* **2014**, *6* (8), 2219−2223.

(11) Spöri, C.; Kwan, J. T. H.; Bonakdarpour, A.; Wilkinson, D. P.; Strasser, P. The Stability Challenges of Oxygen Evolving Catalysts:

Towards a Common Fundamental Understanding and Mitigation of Catalyst Degradation. *Angew. Chemie - Int. Ed.* **2017**, *56* (22), 5994−6021.
(12) Böhm, D.; Beetz, M.; Schuster, M.; Peters, K.; Hufnagel, A. G.; Döblinger, M.; Böller, B.; Bein, T.; Fattakhova-Rohlfing, D. Efficient OER Catalyst with Low Ir Volume Density Obtained by Homogeneous Deposition of Iridium Oxide Nanoparticles on Macroporous Antimony-Doped Tin Oxide Support. *Adv. Funct. Mater.* **2020**, *30* (1), 1906670.
(13) Böhm, D.; Beetz, M.; Gebauer, C.; Bernt, M.; Schröter, J.; Kornherr, M.; Zoller, F.; Bein, T.; Fattakhova-Rohlfing, D. Highly Conductive Titania Supported Iridium Oxide Nanoparticles with Low Overall Iridium Density as OER Catalyst for Large-Scale PEM Electrolysis. *Appl. Mater. Today* **2021**, *24*, No. 101134.
(14) Möckl, M.; Ernst, M. F.; Kornherr, M.; Allebrod, F.; Bernt, M.; Byrknes, J.; Eickes, C.; Gebauer, C.; Moskovtseva, A.; Gasteiger, H. A. Durability Testing of Low-Iridium PEM Water Electrolysis Membrane Electrode Assemblies. *J. Electrochem. Soc.* **2022**, *169*, No. 064505.
(15) Hu, W.; Chen, S.; Xia, Q. IrO_2/Nb−TiO_2 Electrocatalyst for Oxygen Evolution Reaction in Acidic Medium. *Int. J. Hydrogen Energy* **2014**, *39* (13), 6967−6976.
(16) Hao, C.; Lv, H.; Zhao, Q.; Li, B.; Zhang, C.; Mi, C.; Song, Y.; Ma, J. Investigation of V-Doped TiO_2 as an Anodic Catalyst Support for SPE Water Electrolysis. *Int. J. Hydrogen Energy* **2017**, *42* (15), 9384−9395.
(17) Siracusano, S.; Baglio, V.; D'Urso, C.; Antonucci, V.; Aricò, A. S. Preparation and Characterization of Titanium Suboxides as Conductive Supports of IrO_2 Electrocatalysts for Application in SPE Electrolysers. *Electrochim. Acta* **2009**, *54* (26), 6292−6299.
(18) Wang, L.; Lettenmeier, P.; Golla-Schindler, U.; Gazdzicki, P.; Cañas, N. A.; Morawietz, T.; Hiesgen, R.; Hosseiny, S. S.; Gago, A. S.; Friedrich, K. A. Nanostructured Ir-Supported on Ti_4O_7 as a Cost-Effective Anode for Proton Exchange Membrane (PEM) Electrolyzers. *Phys. Chem. Chem. Phys.* **2016**, *18* (6), 4487−4495.
(19) Chen, G.; Bare, S. R.; Mallouk, T. E. Development of Supported Bifunctional Electrocatalysts for Unitized Regenerative Fuel Cells. *J. Electrochem. Soc.* **2002**, *149* (8), A1092−A1099.
(20) Regonini, D.; Adamaki, V.; Bowen, C. R.; Pennock, S. R.; Taylor, J.; Dent, A. C. E. AC Electrical Properties of TiO_2 and Magnéli Phases, Ti_nO_{2n-1}. *Solid State Ionics* **2012**, *229*, 38−44.
(21) Slavcheva, E.; Borisov, G.; Lefterova, E.; Petkucheva, E.; Boshnakova, I. Ebonex Supported Iridium as Anode Catalyst for PEM Water Electrolysis. *Int. J. Hydrogen Energy* **2015**, *40* (35), 11356−11361.
(22) Pushkarev, A. S.; Pushkareva, I. V.; Du Preez, S. P.; Ivanova, N.; Grigoriev, S.; Slavcheva, E. P.; Bessarabov, D. G.; Fateev, V. N.; Aliyev, A. S. Iridium Catalyst Supported on Conductive Titanium Oxides for Polymer Electrolyte Membrane Electrolysis. *Chem. Probl.* **2019**, *17* (1), 9−15.
(23) Kasian, O. I.; Luk'yanenko, T. V.; Demchenko, P.; Gladyshevskii, R. E.; Amadelli, R.; Velichenko, A. B. Electrochemical Properties of Thermally Treated Platinized Ebonex® with Low Content of Pt. *Electrochim. Acta* **2013**, *109*, 630−637.
(24) Afifi, M. A.; Abdel-Aziz, M. M.; Yahia, I. S.; Fadel, M.; Wahab, L. A. Transport Properties of Polycrystalline TiO_2 and Ti_2O_3 as Semiconducting Oxides. *J. Alloys Compd.* **2008**, *455* (1−2), 92−97.
(25) Chen, C. C.; Chen, J. H.; Chao, C. G.; Say, W. C. Electrochemical Characteristics of Surface of Titanium Formed by Electrolytic Polishing and Anodizing. *J. Mater. Sci.* **2005**, *40* (15), 4053−4059.
(26) Bernt, M.; Gasteiger, H. A. Influence of Ionomer Content in IrO_2/TiO_2 Electrodes on PEM Water Electrolyzer Performance. *J. Electrochem. Soc.* **2016**, *163* (11), F3179−F3189.
(27) Bernt, M.; Schramm, C.; Schröter, J.; Gebauer, C.; Byrknes, J.; Eickes, C.; Gasteiger, H. A. Effect of the IrO_x Conductivity on the Anode Electrode/Porous Transport Layer Interfacial Resistance in PEM Water Electrolyzers. *J. Electrochem. Soc.* **2021**, *168* (8), No. 084513.
(28) Endo, K.; Katayama, Y.; Miura, T.; Kishi, T. Composition Dependence of the Oxygen-Evolution Reaction Rate on $Ir_xTi_{1-x}O_2$ Mixed-Oxide Electrodes. *J. Appl. Electrochem.* **2002**, *32* (2), 173−178.
(29) Bernsmeier, D.; Bernicke, M.; Schmack, R.; Sachse, R.; Paul, B.; Bergmann, A.; Strasser, P.; Ortel, E.; Kraehnert, R. Oxygen Evolution Catalysts Based on Ir−Ti Mixed Oxides with Templated Mesopore Structure: Impact of Ir on Activity and Conductivity. *ChemSusChem* **2018**, *11* (14), 2367−2374.
(30) Frisch, M.; Raza, M. H.; Ye, M. Y.; Sachse, R.; Paul, B.; Gunder, R.; Pinna, N.; Kraehnert, R. ALD-Coated Mesoporous Iridium-Titanium Mixed Oxides: Maximizing Iridium Utilization for an Outstanding OER Performance. *Adv. Mater. Interfaces* **2022**, *9* (6), 1−11.
(31) Kasian, O.; Li, T.; Mingers, A. M.; Schweinar, K.; Savan, A.; Ludwig, A.; Mayrhofer, K. Stabilization of an Iridium Oxygen Evolution Catalyst by Titanium Oxides. *J. Phys. Energy* **2021**, *3* (3), No. 034006.
(32) Schuppert, A. K.; Topalov, A. A.; Katsounaros, I.; Klemm, S. O.; Mayrhofer, K. J. J. A Scanning Flow Cell System for Fully Automated Screening of Electrocatalyst Materials. *J. Electrochem. Soc.* **2012**, *159* (11), F670−F675.
(33) Grote, J. P.; Zeradjanin, A. R.; Cherevko, S.; Mayrhofer, K. J. J. Coupling of a Scanning Flow Cell with Online Electrochemical Mass Spectrometry for Screening of Reaction Selectivity. *Rev. Sci. Instrum.* **2014**, *85* (10), 104101.
(34) Kasian, O.; Geiger, S.; Schalenbach, M.; Mingers, A. M.; Savan, A.; Ludwig, A.; Cherevko, S.; Mayrhofer, K. J. J. Using Instability of a Non-Stoichiometric Mixed Oxide Oxygen Evolution Catalyst As a Tool to Improve Its Electrocatalytic Performance. *Electrocatalysis* **2018**, *9* (2), 139−145.
(35) Kasian, O.; Geiger, S.; Stock, P.; Polymeros, G.; Breitbach, B.; Savan, A.; Ludwig, A.; Cherevko, S.; Mayrhofer, K. J. J. On the Origin of the Improved Ruthenium Stability in RuO 2 − IrO 2 Mixed Oxides. *J. Electrochem. Soc.* **2016**, *163* (11), F3099−F3104.
(36) Schuppert, A. K.; Topalov, A. A.; Savan, A.; Ludwig, A.; Mayrhofer, K. J. J. Composition-Dependent Oxygen Reduction Activity and Stability of Pt-Cu Thin Films. *ChemElectroChem.* **2014**, *1* (2), 358−361.
(37) Knöppel, J.; Möckl, M.; Escalera-López, D.; Stojanovski, K.; Bierling, M.; Böhm, T.; Thiele, S.; Rzepka, M.; Cherevko, S. On the Limitations in Assessing Stability of Oxygen Evolution Catalysts Using Aqueous Model Electrochemical Cells. *Nat. Commun.* **2021**, *12*, 2231.
(38) Cherevko, S.; Reier, T.; Zeradjanin, A. R.; Pawolek, Z.; Strasser, P.; Mayrhofer, K. J. J. Stability of Nanostructured Iridium Oxide Electrocatalysts during Oxygen Evolution Reaction in Acidic Environment. *Electrochem. commun.* **2014**, *48*, 81−85.
(39) Kasian, O.; Grote, J. P.; Geiger, S.; Cherevko, S.; Mayrhofer, K. J. J. The Common Intermediates of Oxygen Evolution and Dissolution Reactions during Water Electrolysis on Iridium. *Angew. Chemie - Int. Ed.* **2018**, *57* (9), 2488−2491.
(40) Kasian, O.; Geiger, S.; Li, T.; Grote, J. P.; Schweinar, K.; Zhang, S.; Scheu, C.; Raabe, D.; Cherevko, S.; Gault, B.; Mayrhofer, K. J. J. Degradation of Iridium Oxides via Oxygen Evolution from the Lattice: Correlating Atomic Scale Structure with Reaction Mechanisms. *Energy Environ. Sci.* **2019**, *12* (12), 3548−3555.
(41) Schweinar, K.; Gault, B.; Mouton, I.; Kasian, O. Lattice Oxygen Exchange in Rutile IrO_2 during the Oxygen Evolution Reaction. *J. Phys. Chem. Lett.* **2020**, *11* (13), 5008−5014.
(42) Geiger, S.; Kasian, O.; Shrestha, B. R.; Mingers, A. M.; Mayrhofer, K. J. J.; Cherevko, S. Activity and Stability of Electrochemically and Thermally Treated Iridium for the Oxygen Evolution Reaction. *J. Electrochem. Soc.* **2016**, *163* (11), F3132−F3138.
(43) Geiger, S.; Kasian, O.; Ledendecker, M.; Pizzutilo, E.; Mingers, A. M.; Fu, W. T.; Diaz-Morales, O.; Li, Z.; Oellers, T.; Fruchter, L.; Ludwig, A.; Mayrhofer, K. J. J.; Koper, M. T. M.; Cherevko, S. The Stability Number as a Metric for Electrocatalyst Stability Benchmarking. *Nat. Catal.* **2018**, *1* (7), 508−515.

https://doi.org/10.1021/acscatal.3c02948
ACS Catal. 2023, 13, 15427−15438

(44) Qiao, R.; Li, Q.; Zhuo, Z.; Sallis, S.; Fuchs, O.; Blum, M.; Weinhardt, L.; Heske, C.; Pepper, J.; Jones, M.; Brown, A.; Spucces, A.; Chow, K.; Smith, B.; Glans, P. A.; Chen, Y.; Yan, S.; Pan, F.; Piper, L. F. J.; Denlinger, J.; Guo, J.; Hussain, Z.; Chuang, Y. D.; Yang, W. High-Efficiency in Situ Resonant Inelastic x-Ray Scattering (IRIXS) Endstation at the Advanced Light Source. *Rev. Sci. Instrum.* **2017**, *88* (3), No. 033106.
(45) Tanuma, S.; Powell, C. J.; Penn, D. R. Calculations of Electron Inelastic Mean Free Paths. IX. Data for 41 Elemental Solids over the 50 EV to 30 KeV Range. *Surf. Interface Anal.* **2011**, *43* (3), 689−713.
(46) Tanuma, S.; Powell, C. J.; Penn, D. R. Calculations of Electron Inelastic Mean Free Paths. V. Data for 14 Organic Compounds over the 50−2000 EV Range. *Surf. Interface Anal.* **1994**, *21* (3), 165−176.
(47) Tougaard, S. M. *QUASES-Inelastic Electron Mean Free Path Calculator (by TPP2M Formula)*, 2021. DOI: 10.5281/zenodo.5707501.
(48) Ueda, S.; Katsuya, Y.; Tanaka, M.; Yoshikawa, H.; Yamashita, Y.; Ishimaru, S.; Matsushita, Y.; Kobayashi, K. Present Status of the NIMS Contract Beamline BL15XU at SPring-8. *AIP Conf. Proc.* **2010**, *1234*, 403−406.
(49) Moulder, J. F.; Stickle, W. F.; Sobol, P. E.; Bomben, K. D. *Handbook of X-Ray Photoelectron Spectroscopy; A Reference Book of Standard Spectra for Identification and Interpretation of XPS Data*; Chastain, J. Ed.; Perkin-Elmer Corp.: Eden Prairie, MN, 1992.
(50) Werner, W.; Smekal, W.; Powell, C. J.; Gorham, J. *Simulation of Electron Spectra for Surface Analysis (SESSA) - Version 2.1*. National Institute of Standards and Technology: Gaithersburg, MD, 2021 DOI: 10.6028/NIST.NSRDS.100-2021.
(51) Major, G. H.; Shah, D.; Avval, T. G.; Fernandez, V.; Fairley, N.; Linford, M. R. Advanced Line Shapes in X-Ray Photoelectron Spectroscopy II. The Finite Lorentzian (LF) Line Shape. *Vac. Technol. Coat.* **2020**, 35−40.
(52) Trzhaskovskaya, M. B.; Nefedov, V. I.; Yarzhemsky, V. G. Photoelectron Angular Distribution Parameters for Elements Z = 1 to Z = 54 in the Photoelectron Energy Range 100−5000 EV. *At. Data Nucl. Data Tables* **2001**, *77* (1), 97−159.
(53) Trzhaskovskaya, M. B.; Nefedov, V. I.; Yarzhemsky, V. G. Photoelectron Angular Distribution Parameters for Elements Z = 55 to Z = 100 in the Photoelectron Energy Range 100−5000 EV. *At. Data Nucl. Data Tables* **2002**, *82* (2), 257−311.
(54) Nyholm, R.; Martensson, N.; Lebugle, A.; Axelsson, U. Auger and Coster-Kronig Broadening Effects in the 2p and 3p Photoelectron Spectra from the Metals ^{22}Ti-^{30}Zn. *J. Phys. F Met. Phys.* **1981**, *11* (8), 1727−1733.
(55) de Groot, F.; Kotani, A. *Core Level Spectroscopy of Solids*; CRC Press: Boca Raton, 2008. DOI: 10.1201/9781420008425.
(56) Newville, M.; Stensitzki, T.; Allen, D. B.; Rawlik, M.; Ingargiola, A.; Nelson, A. LMFIT: Non-Linear Least-Square Minimization and Curve-Fitting for Python. *Astrophys. Source Code Library* **2016**, pp.ascl-1606 DOI: .
(57) Pfeifer, V.; Jones, T. E.; Velasco Vélez, J. J.; Massué, C.; Arrigo, R.; Teschner, D.; Girgsdies, F.; Scherzer, M.; Greiner, M. T.; Allan, J.; Hashagen, M.; Weinberg, G.; Piccinin, S.; Hävecker, M.; Knop-Gericke, A.; Schlögl, R. The Electronic Structure of Iridium and Its Oxides. *Surf. Interface Anal.* **2016**, *48* (5), 261−273.
(58) Pfeifer, V.; Jones, T. E.; Velasco-Vélez, J. J.; Massué, C.; Greiner, M. T.; Arrigo, R.; Teschner, D.; Girgsdies, F.; Scherzer, M.; Allan, J.; Hashagen, M.; Weinberg, G.; Piccinin, S.; Hävecker, M.; Knop-Gericke, A.; Schlögl, R. The Electronic Structure of Iridium Oxide Electrodes Active in Water Splitting. *Phys. Chem. Chem. Phys.* **2016**, *18* (4), 2292−2296.
(59) Saveleva, V. A.; Wang, L.; Teschner, D.; Jones, T.; Gago, A. S.; Friedrich, K. A.; Zafeiratos, S.; Schlögl, R.; Savinova, E. R. Operando Evidence for a Universal Oxygen Evolution Mechanism on Thermal and Electrochemical Iridium Oxides. *J. Phys. Chem. Lett.* **2018**, *9* (11), 3154−3160.
(60) Velasco-Vélez, J.; Carbonio, E.; Chuang, C. H.; Hsu, C. J.; Lee, J. F.; Arrigo, R.; Hävecker, M.; Wang, R.; Plodinec, M.; Centeno, A.; Zurutuza, A.; Falling, L. J.; Mom, R.; Hofmann, S.; Schlögl, R.; Knop-Gericke, A.; Jones, T. *Surface Constrained Electron-Hole Rich Species Active in the Electrocatalytic Water Splitting*. 2020. .
(61) Thompson, Y.; Polzer, M.; Gonzalez-Gutierrez, J.; Kasian, O.; Heckl, J. P.; Dalbauer, V.; Kukla, C.; Felfer, P. J. Fused Filament Fabrication-Based Additive Manufacturing of Commercially Pure Titanium. *Adv. Eng. Mater.* **2021**, *23* (12), 2100380.
(62) Pham, C. V.; Bühler, M.; Knöppel, J.; Bierling, M.; Seeberger, D.; Escalera-López, D.; Mayrhofer, K. J. J.; Cherevko, S.; Thiele, S. IrO_2 Coated TiO_2 Core-Shell Microparticles Advance Performance of Low Loading Proton Exchange Membrane Water Electrolyzers. *Appl. Catal. B* **2020**, *269*, No. 118762.
(63) Crocombette, J. P.; Jollet, F. Ti 2p X-Ray Absorption in Titanium Dioxides (TiO_2): The Influence of the Cation Site Environment. *J. Phys.: Condens. Matter* **1994**, *6* (49), 10811−10821.
(64) Henderson, G. S.; Liu, X.; Fleet, M. E. A Ti L-Edge X-Ray Absorption Study of Ti-Silicate Glasses. *Phys. Chem. Miner.* **2002**, *29* (1), 32−42.
(65) de Groot, F. M. F.; Figueiredo, M. O.; Basto, M. J.; Abbate, M.; Petersen, H.; Fuggle, J. C. 2 p X-Ray Absorption of Titanium in Minerals. *Phys. Chem. Miner.* **1992**, *19* (3), 140−147.
(66) Van Der Laan, G.; Mythen, C. S.; Padmore, H. A. Electronic Polaron Excitations in the X-Ray Absorption Spectrum of TiO_2. *Europhys. Lett. (EPL)* **1990**, *11* (1), 67−72.
(67) Fischer, D. W.; Baun, W. L. Band Structure and the Titanium $L_{II,\ III}$ x-Ray Emission and Absorption Spectra from Pure Metal, Oxides, Nitride, Carbide, and Boride. *J. Appl. Phys.* **1968**, *39* (10), 4757−4776.
(68) Lusvardi, V. S.; Barteau, M. A.; Chen, J. G.; Eng, J.; Frühberger, B.; Teplyakov, A. An NEXAFS Investigation of the Reduction and Reoxidation of TiO_2(001). *Surf. Sci.* **1998**, *397* (1−3), 237−250.
(69) Li, J.; Liu, C. H.; Li, X.; Wang, Z. Q.; Shao, Y. C.; Wang, S. D.; Sun, X. L.; Pong, W.-F.; Guo, J. H.; Sham, T.-K. Unraveling the Origin of Visible Light Capture by Core−Shell TiO_2 Nanotubes. *Chem. Mater.* **2016**, *28* (12), 4467−4475.
(70) Kronawitter, C. X.; Bakke, J. R.; Wheeler, D. A.; Wang, W. C.; Chang, C.; Antoun, B. R.; Zhang, J. Z.; Guo, J.; Bent, S. F.; Mao, S. S.; Vayssieres, L. Electron Enrichment in 3d Transition Metal Oxide Hetero-Nanostructures. *Nano Lett.* **2011**, *11* (9), 3855−3861.
(71) Hsu, M. Y.; Yang, W. C.; Teng, H.; Leu, J. Microstructure and Composition of TiO_2 Nanotube Arrays Fabricated with HF and NH_4F Electrolytes and Their Evolution during Annealing. *J. Electrochem. Soc.* **2011**, *158* (3), K81.
(72) Bian, Y.; Li, T.; Weaver, J. F. Structure and Reactivity of Iridium Oxide Layers Grown on Ir (1 0 0) by Oxidation at Sub-Ambient O_2 Pressures. *J. Phys. D. Appl. Phys.* **2019**, *52* (43), 434002.
(73) Li, T.; Kim, M.; Liang, Z.; Asthagiri, A.; Weaver, J. F. Dissociative Chemisorption and Oxidation of H_2 on the Stoichiometric IrO_2(110) Surface. *Top. Catal.* **2018**, *61* (5−6), 397−411.
(74) Liu, Z.; Welsch, G. Literature Survey on Diffusivities of Oxygen, Aluminum, and Vanadium in Alpha Titanium, Beta Titanium, and in Rutile. *Metall. Trans. A* **1988**, *19* (4), 1121−1125.
(75) Armentrout, P. B.; Li, F. X. Bond Energy of IrO^+: Guided Ion-Beam and Theoretical Studies of the Reaction of Ir^+ (^{5}F) with O_2. *J. Phys. Chem. A* **2013**, *117* (33), 7754−7766.
(76) da Silva, L.; Alves, V.; de Castro, S.; Boodts, J. F. XPS Study of the State of Iridium, Platinum, Titanium and Oxygen in Thermally Formed IrO_2+TiO_2+PtO_x Films. *Colloids Surfaces A Physicochem. Eng. Asp.* **2000**, *170* (2−3), 119−126.

https://doi.org/10.1021/acscatal.3c02948
ACS Catal. 2023, 13, 15427−15438